Environmental Surface Stability of the $MAPbBr_3$ Single Crystal

Congcong Wang,[†] Benjamin R. Ecker,[†] Haotong Wei,[‡] Jinsong Huang,[‡] and Yongli Gao*[,†]

[†]Department of Physics and Astronomy, University of Rochester, Rochester, New York 14627, United States

[‡]Department of Applied Physical Sciences, University of North Carolina at Chapel Hill, Chapel Hill, North Carolina 27599, United States

ABSTRACT: Organic−inorganic halide perovskites have emerged as a promising semiconductor family because of their remarkable performance in optoelectronic devices. On the other hand, the stability of perovskites remains a critical issue. In this work, we report a quantitative and systematic investigation of in situ cleaved $MAPbBr_3$ single-crystal degradation processes in X-ray, N_2, O_2, and H_2O environments. The high-quality crystals were monitored by high-resolution X-ray photoelectron spectroscopy with careful control of the exposure time and pressure. The detailed electronic structure and compositional changes of the crystal were tracked throughout the different exposures, and these studies provided insights into the various degradation mechanisms. We identified that ∼10% of the surface $MAPbBr_3$ degraded to metallic lead under X-rays in vacuum, while N_2 could protect the sample from the degradation for 9 h under the same condition. Other measurements showed that while the surface was not sensitive to pure O_2, it was susceptible to H_2O exposure within the top 0.37 nm and a reaction threshold of $\sim 10^8$ Langmuir was found. Below the threshold, H_2O acted only as an n-type dopant; above it, the surface began to decompose. These observations highlight possible future directions to improve the material stability by environmental control.

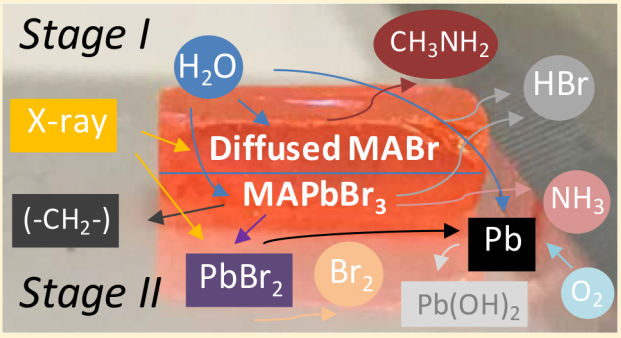

INTRODUCTION

Hybrid organometal halide perovskites have attracted considerable attention in the past few years, with remarkable power conversion efficiency (PCE) rising from 3.8 to over 22%.[1−8] In particular, methylammonium lead halide perovskites, namely, $CH_3NH_3PbX_3$ ($MAPbX_3$), have unique properties such as a long diffusion length, low carrier effective masses, high absorption coefficients, and low-cost fabrication processes.[9−13] These characteristics have expanded the applications of $MAPbX_3$ beyond photovoltaic devices to light-emitting diodes and photodetectors.[14−16] However, the stability of perovskites remains a critical issue, and it can impede future developments and applications of perovskite-based devices. The degradations have been intensively investigated at the device level,[17−22] but few measurements have been made at the surface analytical level to understand the intrinsic properties and degradation processes of the materials.[6,11,23−25] As a result, the mechanisms of the degradation are still under debate. A complete understanding of the degradation processes is necessary for widespread photovoltaic and other potential applications of the perovskites.

A number of studies have been made to determine the factors that induce the degradation of perovskites. Grätzel and co-workers found that the device should be fabricated under controlled atmospheric conditions with a humidity of <1%.[26] Niu's group reported that moisture catalyzed the decomposition of the $MAPbI_3$ layer.[27] Boyen's group demonstrated that significant structural changes occurred during the annealing of $MAPbI_3$ at 85 °C in different atmospheres.[28] Our previous work revealed that $MAPbI_3$ was not sensitive to O_2 but started to decompose after $\sim 2 \times 10^{10}$ Langmuir of H_2O exposure.[24,25,29] Other factors, such as voltage,[30] light,[23,31−33] and I_2 vapor,[34] have also been investigated.

Similar to the iodine perovskite, $MAPbBr_3$ is considered to be another promising perovskite material for optoelectronics and photovoltaics.[16,35−38] With higher hole mobility, $MAPbBr_3$ has certain advantages in comparison with $MAPbI_3$. The sensitive and low-cost X-ray detectors made of $MAPbBr_3$ single crystals (SCs) have been demonstrated to possess an extremely small surface charge recombination velocity and extended diffusion length.[16] Additionally, reports have suggested that $MAPbBr_3$ has a better stability in air than $MAPbI_3$.[39−41] However, to date, no systematic degradation study has been performed to investigate the stability of $MAPbBr_3$ in different environments at the surface analytical level. Either the degradation rate or the decomposition mechanism upon exposure is yet to be known. Most previous studies on the perovskite stability have typically been carried out under ambient conditions without quantitative control of environmental factors, and it is difficult to compare the results from different laboratories and gain insights into the intrinsic decomposition mechanisms.

Received: December 27, 2017
Revised: January 20, 2018
Published: January 23, 2018

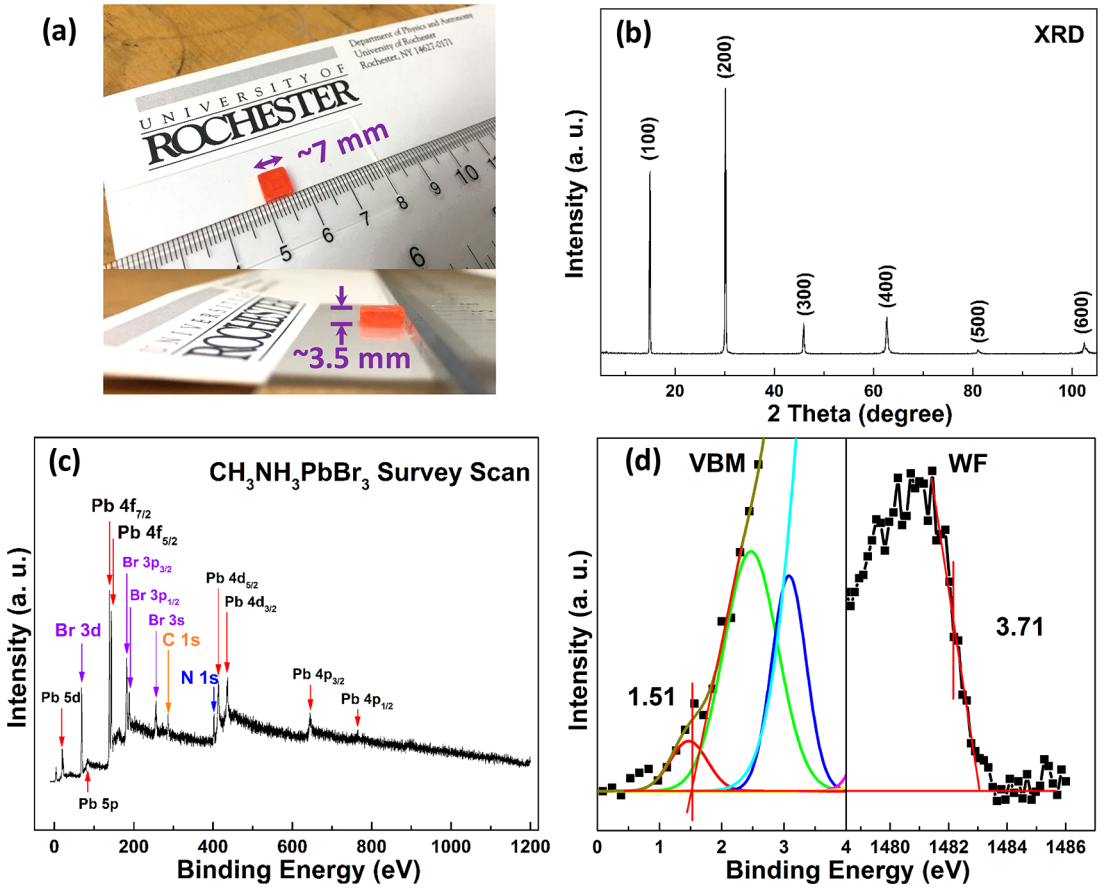

Figure 1. (a) $MAPbBr_3$ single crystal. (b) XRD pattern of the as-grown single crystal. (c) HR-XPS survey scan. (d) Valence band region and cutoff region. All spectra were normalized for visual clarity with an arbitrary unit of intensity.

In this work, we report a quantitative and systematic investigation of in situ cleaved $MAPbBr_3$ SC degradation processes in X-ray, N_2, O_2, and H_2O environments. X-ray diffraction (XRD), atomic force microscopy (AFM), and scanning electron microscopy (SEM) were used to confirm the high quality of the crystal and monitor the morphological changes. Most exposure measurements were performed in ultrahigh vacuum (UHV), with different environmental factors carefully controlled. The exposure to gases was measured in Langmuir (L, 1 L = 10^{-6} Torr·s). We revealed the detailed electronic structure and compositional changes of the crystal during different exposures with high-resolution X-ray photoelectron spectroscopy (HR-XPS).

EXPERIMENTAL SECTION

$MAPbBr_3$ Single Crystal Preparation. High-quality methylammonium lead bromide perovskite single crystals were synthesized by a solution-processed antisolvent growth method as described in ref 16. Briefly, 0.64 M $PbBr_2$ and 0.8 M MABr were dissolved in 5 mL of *N*,*N*-dimethylformamide solution in a small vial. Then the vial was sealed with foil but left with a small hole to let dichloromethane slowly get in. Dichloromethane was employed as an antisolvent to precipitate the SCs. Finally, the vial was stored in an atmosphere of dichloromethane, and $MAPbBr_3$ SC slowly grew over 2 days. We then cut the large crystal into small ones with an average size of ~7 mm × 7 mm × 3.5 mm.

$MAPbBr_3$ Single Crystal Cleavage. The same crystal was used in all experiments, but freshly cleaved every time at room temperature. In particular for HR-XPS measurements, the crystals were cleaved in a modified surface science laboratories' SSX-100 UHV system (in situ). For AFM and SEM measurements, the samples were cleaved ex situ. The cleaving technique to acquire high-quality surfaces is shown in Figure S1. The perovskite SC was first glued on top of the Au/Si substrate with silver epoxy (Epoxy Technology, Inc.). Then, a tungsten rod was glued perpendicularly on top of the perovskite surface with a Varian Torr seal. Once the crystal was loaded into the vacuum chamber, the rod was hit by the vacuum valve, and the top surface of the crystal glued together with the rod was cleaved off at the same time. With this method, an in situ cleaved perovskite single crystal (001) surface was achieved. The ex situ cleaving process is about the same but is processed only outside the vacuum chamber. Other details can be found in ref 38.

Exposures. The UHV chamber consists of two interconnected chambers, an exposure chamber for gas exposure and an analyzer chamber for HR-XPS measurements. The base pressures of the exposure chamber and the analyzer chamber are typically 1×10^{-5} and 1×10^{-11} Torr, respectively. For the X-ray exposure, the sample was monitored under HR-XPS for 10 continuous hours. For the nitrogen and oxygen exposures, high-purity 4.8 grade N_2 and ultrapure carrier-grade O_2 from Airgas Inc. were used in controlled steps from 1 to 10^{12} and 10^{10} L, respectively. The exposures up to 10^5 L were carried out in the analyzer chamber. The rest were performed in the exposure chamber, and the samples were transferred to the analyzer chamber for HR-XPS measurements after each

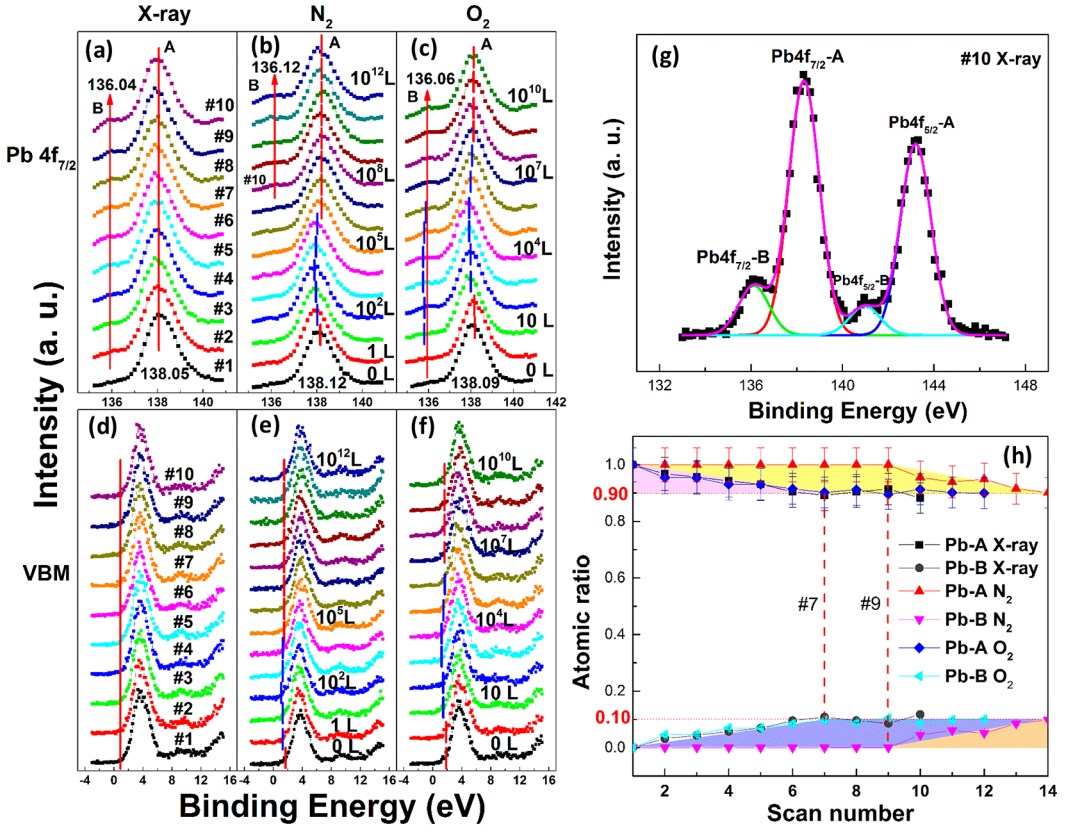

Figure 2. Evolutions of Pb $4f_{7/2}$ peaks under (a) X-ray, (b) N_2, and (c) O_2 exposures. Evolutions of VBM under (d) X-ray, (e) N_2, and (f) O_2 exposures. (g) The detailed fitting curves of Pb $4f_{7/2}$-A, Pb $4f_{7/2}$-B, Pb $4f_{5/2}$-A, and Pb $4f_{5/2}$-B peaks under the no. 10 X-ray scan. (h) Atomic ratio comparisons of lead peaks under the three conditions with error bars.

exposure step. Marks were made on the sample holder to make sure the measurement was performed at the same position every time. The H_2O exposure was administered with a clean glass tube half filled with deionized water, connected to the exposure chamber through a microleak valve. The tube was pumped repeatedly to ensure that it was filled with pure H_2O vapor. The pressure was adjusted from 1×10^{-4} to 15 Torr to keep the H_2O exposure time manageable. All measurements were performed at room temperature.

Calculation of the X-ray Dose. The surface composition and the electronic structure of perovskite SCs were measured by HR-XPS with a monochromatic Al Kα source (1486.6 eV). The energy resolution is about 0.6 eV. HR-XPS is a surface-sensitive technique, and the mean free path is only 2.0 nm in our UHV chamber. All of the spectra were fitted after subtracting the background with a Shirley-type correction. The ratio of the Lorentzian and Gaussian fittings was not fixed during the peak fitting. The atomic ratios of the crystals were calculated by dividing the fitted peak areas by the atomic sensitive factors (ASF) of the instrument. The X-ray spot size on the sample is about 0.1 mm in diameter. The voltage and the current of the X-ray gun are 10 kV and 20.6 mA, respectively. The current of the sample under X-ray irradiation is 0.00008 μA. Each set of spectral scans (C 1s, N 1s, Pb $4f_{7/2}$, Br $3d_{5/2}$, O 1s, VB, cutoff) took about 1 h to complete. The X-ray dose was roughly calculated by the Gy unit (gray, = J/kg). The power of the X-ray on the sample was 10 kV $\times$ 0.0008 μA = 8×10^{-7} J s^{-1}. With a scan time of 3600 s and a perovskite mass of $\pi \times \left(\frac{0.01cm}{2}\right)^2 \times 79cm^2g^{-1} = 9.94 \times 10^{-7}g$,[42] the dose was estimated as $\frac{8 \times 10^{-7}\ \mathrm{J\ s^{-1}} \times 3600\ \mathrm{s}}{9.94 \times 10^{-7}\mathrm{g}} = 2.90 \times 10^3$ Gy for each set of scans.

Characterization. The morphological properties were investigated with an NTMDT AFM microscope in tapping mode and a Zeiss Auriga SEM. The crystalline structure of $MAPbBr_3$ was identified by XRD collected with a Philips APD diffractometer. The XRD diffractometer was equipped with a Cu Kα X-ray tube operating at 40 kV and 30 mA using a step size of 0.050° and a time per step of 0.5 s. The as-grown SC was mounted on a low-background holder. Each measurement took about 0.5 h. Experimental fitting of the X-ray data was carried out from 5 to 105° 2θ at a fixed ω angle of 0.5°.

RESULTS AND DISCUSSION

Characterization of the $MAPbBr_3$ Single Crystal. Figure 1a shows the as-grown perovskite SC with an average area of 7 mm × 7 mm. The thickness of the sample is ~3.5 mm. The XRD result confirmed the (001) surface and the highly crystalline cubic structure of the pristine crystal (Figure 1b). The lattice parameter derived from the XRD result is 5.93 Å, consistent with other reports.[38,43,44] The as-cleaved surfaces examined with SEM and energy dispersive spectroscopy (EDS) are shown in Figure S2a,b. The surface is mirrorlike and featureless, confirming the high quality of the sample. The EDS result shows the existence of Pb and Br. The HR-XPS survey scan of the in situ cleaved perovskite single crystal is shown in Figure 1c. All of the perovskite core levels are marked in the spectrum. A small amount of an oxygen impurity was observed on the freshly cleaved surface, but the signal intensity of O 1s is

Table 1. Atomic Ratio Comparisons of the Two Spots under X-ray Exposure

spot	C	N	Pb-A	Pb-B	Br	O
control spot (as-cleaved)	1.72 ± 0.10	0.91 ± 0.05	1	0	2.79 ± 0.17	0.29 ± 0.02
control spot (second scan, 10 h)	1.87 ± 0.11	1.03 ± 0.06	0.99	0.01	2.98 ± 0.18	0.28 ± 0.02
test spot (as-cleaved)	1.78 ± 0.11	0.88 ± 0.05	1	0	2.84 ± 0.17	0.17 ± 0.01
test spot (second scan)	1.98 ± 0.12	0.97 ± 0.06	0.99	0.01	2.96 ± 0.18	0.17 ± 0.01
test spot (after 10 h)	2.64 ± 0.16	1.15 ± 0.07	0.90	0.10	3.33 ± 0.20	0.15 ± 0.01
control spot net change	9 ± 0.54%	13 ± 0.78%	−1%	1%	7 ± 0.42%	
test spot (second scan)	11 ± 0.66%	10 ± 0.60%	−1%	1%	4 ± 0.24%	
test spot net change	48 ± 2.88%	31 ± 1.86%	−10%	10%	17 ± 1.02%	

too small to be identified in the survey scan. Detailed photoelectron spectroscopy figures for the individual elements are presented in Figure S3. The elemental ratio is C/N/Pb/Br/O = 1.61:1.12:1.00:2.89:0.17. Here, Pb is taken as the unit. This ratio is close to the stoichiometric value. The small amounts of excess carbon, nitrogen, and oxygen may have come from the residual reactants used in the crystal growth process. The atomic ratios of the cleaved crystal used in X-ray, N_2, O_2, and H_2O exposure studies are listed in Table S1.

Figure 1d shows the vacuum-level cutoff region and the valence band (VB) region of the sample measured by HR-XPS. The binding energy (BE) is referenced to the Fermi level (E_F) of the material. The cutoff energy is determined by the inflection point of the sharp change region of the cutoff spectrum. The vacuum level (VL) is obtained from the difference between the photon energy (1486.6 eV) and the cutoff energy. The VL of $MAPbBr_3$ SC is measured to be 3.71 eV above the E_F, and the value represents the work function (WF). In our previous work, we reported the band gap of the SC to be 2.3 eV.[38] The valence band maximum (VBM) obtained using linear extrapolation[45−48] is 1.51 eV below the E_F. This indicates that the crystal surface presents slight n-type semiconductor behavior.

X-ray Exposure. HR-XPS is the main technique used to quantify the elemental ratio and the electronic structure changes of perovskite single crystals. Moreover, $MAPbBr_3$ SCs were reported to be used as sensitive X-ray detectors.[16,49]

The effect of the X-ray on the samples during the measurements should be examined before further investigations on the degradation process of $MAPbBr_3$ by environmental gas exposure. Therefore, we first performed the X-ray exposure on a freshly cleaved perovskite. Two spots were marked on the surface for comparison. The test spot was exposed to HR-XPS for 10 h continuously, while the control spot was measured only before and after 10 h in UHV and darkness. It took about 1 h for each set of the complete spectral scans (C 1s, N 1s, Pb $4f_{7/2}$, Br $3d_{5/2}$, O 1s, VB, cutoff), and we did 10 sets of scans at the test spot and 2 sets of scans at the control spot.

Figure 2a,d shows the evolutions of the Pb $4f_{7/2}$ peaks and the VBM at the test spot. All of the spectra were normalized to the same height for visual clarity. Interestingly, a second Pb $4f_{7/2}$ peak (Pb-B) at ∼136.04 eV started to show up from the second scan as denoted by the red arrow in Figure 2a. It is identified to be from metallic Pb, while the Pb-A at ∼138.05 eV is from the perovskite. The detailed fitting of the 10th scan of Pb $4f_{7/2}$ and Pb $4f_{5/2}$ peaks is shown in Figure 2g. The evolution of other elements under X-ray exposure can be found in Figure S4. Beside that of Pb, there is no discernible change in the core levels of all elements and the VBM within the instrumental uncertainty. For both the control spot and the test spot, there is a small amount of metallic Pb that showed up after the second scan. The other core levels and the VBM did not change.

To quantify the process, we examined the evolution of the intensities of the core levels and suggest the mechanism of the degradation process as follows:

$$CH_3NH_3PbBr_3 \xrightarrow{\text{X-ray}} CH_3NH_3Br + Pb + Br_2 \uparrow \text{(in UHV)} \quad (1)$$

The atomic ratio comparisons of the two spots are listed in Table 1. Here, the sum of the intensities of Pb-A and Pb-B was used as the basis. The control spot was exposed to X-rays for 2 h, which is the same amount of exposure as the second scan at the test spot. Despite having stayed under vacuum for 8 more hours, the ratio changes at the control spot are almost the same as those at the test spot in the second scan, indicating no vacuum degradation.

At the test spot, 10% Pb-A degraded to Pb-B, which illustrates that 10% of the perovskite degraded under X-ray exposure after 10 h scans. From the calculation of eq 1, there should be a 10% increase in C 1s and N 1s and a 10% decrease in Br $3d_{5/2}$. However, in Table 1, we showed that C 1s, N 1s, and Br 3d increased ∼48, 31, and 17%, respectively. This suggests that increases of ∼38, 21, and 27% in C 1s, N 1s, and Br 3d, respectively, may come from the MABr diffusion from the bulk to the surface during the 10 h X-ray exposure. The ratios of O 1s are about the same before and after being left in the dark for 10 h at the control spot. It is noteworthy that the C 1s peak position is ∼285.81 eV and no amorphous carbon showed up at ∼284.6 eV at either the test spot (Figure S4) or the control spot (Figure S5). It further confirmed that the increased carbon may come from the diffusion from the bulk but not from the contamination in the UHV chamber. In Figure S2c,d, we compared the surface structures of the as-cleaved sample and the one left in the UHV chamber for 72 h with no light. Plenty of small particles aggregated on the

Table 2. Atomic Ratio Change Comparisons of Perovskite under Different Atmospheres

exposure	C	N	Pb-A	Pb-B	Br	O
X-ray (7 h[a])	35 ± 2.10%	19 ± 1.14%	−10%	10%	15 ± 0.90%	0
X-ray (10 h)	48 ± 2.88%	31 ± 1.86%	−10%	10%	17 ± 1.02%	0
dark 10 h (0 h)	9 ± 0.54%	13 ± 0.78%	−1%	1%	7 ± 0.42%	0
N_2 (10^7 L, 9 h)	0	0	0	0	0	0
N_2 (10^{12} L, 14 h)	20 ± 1.20%[b]	8 ± 0.48%	−10%	10%	−12 ± 0.72%	0
O_2 (10^{10} L, 12 h)	2 ± 0.12%[c]	7 ± 0.42%	−10%	10%	7 ± 0.42%	40 ± 2.40%[d]
H_2O (10^8 L, 7 h)	5 ± 0.30%	−18 ± 0.16%	−10%	10%	−12 ± 0.72%	14 ± 0.84%
H_2O (10^{11} L, 10 h)	88 ± 5.28%	70 ± 4.2%[e]			−15 ± 0.90%	48 ± 2.88%
H_2O net[f] (10^8 L, 7 h)	−30 ± 1.8%	−37 ± 2.22%	0	0	−27 ± 1.62%	14 ± 0.84%
H_2O net[g] (10^{11} L, 10 h)	40 ± 2.4%	−39 ± 2.34%			−32 ± 1.92%	48 ± 2.88%

[a]Hours under HR-XPS scan. [b]Including ∼15% C 1s from perovskite and ∼5% amorphous carbon. [c]Including an ∼37% decrease in C 1s from perovskite and an ∼39% increase from the C−O bond. [d]Including an ∼25% decrease in O 1s from doped O_2 and ∼65% increase from C−O bond. [e]Including an ∼2% increase in N 1s-A (402.11 eV) and an ∼68% increase in N 1s-B (399.98 eV). [f]Ratio change with the subtraction of the test spot net change (X-ray, 7 h). [g]Ratio change with the subtraction of the test spot net change (X-ray, 10 h).

previously flat surface after exposure to vacuum for a long time, which could come from the diffusion of MABr.

N_2 Exposure. Although N_2 is normally used as an inert gas to protect samples or control environmental conditions during the perovskite-relevant experiments,[10,32,50−52] the role of N_2 in the environmental degradation process of the samples still needs to be clarified. To confirm the inert property of the gas, we performed the N_2 exposure on $MAPbBr_3$ from 0 to 10^{12} L and monitored the process with HR-XPS (14 sets of scans, 14 h HR-XPS scan). The evolutions of Pb $4f_{7/2}$ peaks and VBM are shown in Figure 2b,e. Other peaks could be found in Figure S5.

Notably, there were two stages during the exposure process. First, before 10^7 L, an initial p-doping effect of all elements started from the beginning of the exposure as denoted by blue bars, with a maximum shifting at 10^2 L. The peaks then slowly shifted back to the original position at 10^5 L. The VBM followed the same trend and shifted to the lower BE direction by ∼0.31 eV at 10^2 L. These demonstrated that nitrogen p-doped the perovskite crystal merely by physical absorption, and it slowly escaped the surface afterward. There is only one Pb peak from perovskite at 138.12 eV at this stage as shown in Figure 2b. The atomic ratio change in different atmospheres is listed in Table 2. For nitrogen exposure, there is no metallic lead nor ratio change of other elements at 10^7 L with a 9 h HR-XPS scan, indicating that N_2 can protect the surface from HR-XPS X-ray degradation for up to 9 h and prevent the diffusion of MABr at the same time.

Starting from 10^8 L came the second stage, in which the Pb-B peak at ∼136.12 eV rose up. The metallic lead increased to 10% at 10^{12} L (14 h HR-XPS scan), the same amount as for the sample exposed under HR-XPS X-rays for 10 h. Similarly, ∼10% perovskite degraded as shown in Table 2. The decomposition reaction is the same as discussed in eq 1. The excessive 20% carbon includes 15% C 1s from perovskite, and the remaining 5% amorphous carbon showed up from 10^{10} L (Figure S6). The amorphous carbon may come from the absorption of the carbon contamination in the vacuum chamber. There was no extra N 1s and Br $3d_{5/2}$, confirming again that N_2 could prevent the diffusion of MABr from the bulk to the surface. It can be concluded that N_2 as an inert gas could protect the sample from HR-XPS X-ray degradation for 9 h. N_2 first p-doped perovskite by ∼0.31 eV but slowly escaped the crystal. It is advised to use N_2 as the environmental atmosphere when operating perovskite-relevant experiments.

O_2 Exposure. In our previous study of $MAPbI_3$ thin films, O_2 worked only as a p-type dopant during the exposure without reacting with the samples.[25] To compare the performance of the $MAPbBr_3$ SC, we set up the experiment in a similar way and exposed the sample in an O_2 atmosphere from 0 to 10^{10} L. The evolutions of Pb peaks and VBM are shown in Figure 2c,f. Other peaks could be found in Figure S7. As noticed, the metallic lead Pb-B started to show up from the second scan as under the X-ray exposure, which indicated that O_2 could not protect the surface as N_2 did under the same condition.

The change in all peak positions and ratios indicates that there were two stages during the O_2 exposure process. In the first stage, all peaks except O 1s started to shift to the lower BE positions from 1 L and achieved the maximum at 10^4 L. The VBM also followed this trend with a maximum shift of ∼0.18 eV, the same as the O_2 exposures we performed on $MAPbI_3$ thin films. Interestingly, O 1s started to shift to the higher BE direction from the beginning and reached the maximum of ∼534.09 eV at 10^4 L. These strongly suggested that the O 1s signal we detected mostly came from O_2 p-doping at the crystal surface. It is clear that O_2 also p-doped the perovskite SC through physical absorption as N_2 did at this stage.

After 10^4 L in the second stage, the doped O_2 started to bond with C 1s. As shown in Figure S7, a second C 1s at ∼287.71 eV (C 1s-B) and a second O 1s at ∼532.56 eV (O 1s-B) showed up. The detailed ratio analysis can be found in Table 2. C 1s-A (286.07 eV) decreased ∼37% while C 1s-B increased ∼39%. The O 1s peak at ∼534.09 eV (O 1s-A) decreased ∼25% while O 1s-B increased ∼65%. At 10^{10} L, all doped O_2 bonded with C as C−O. With the decrease in the doped O_2, other peaks started to shift back to their original positions. It is worth mentioning that the C 1s that bonded with O 1s came from MA^+ that diffused from the bulk to the surface and also from MABr due to X-ray degradation. There was no direct reaction between perovskite SC and O_2, the performance of which was the same as for the $MAPbI_3$ thin film.

The elemental ratio change comparisons shown in Table 2 demonstrate that after 10^{10} L of O_2 exposure (12 h HR-XPS scan), Pb-B increased 10%, which was again the same as after 10 h of X-ray exposure and 10^{12} L of N_2 exposure (14 h HR-XPS scan). We summarized the evolutions of Pb-A and Pb-B peaks under these three exposures in Figure 2h. The crystal was degraded by X-rays from the first scan if left in vacuum and the O_2 atmosphere, but the degradation started after only nine sets of scans (9 h HR-XPS scan) in the N_2 atmosphere. The

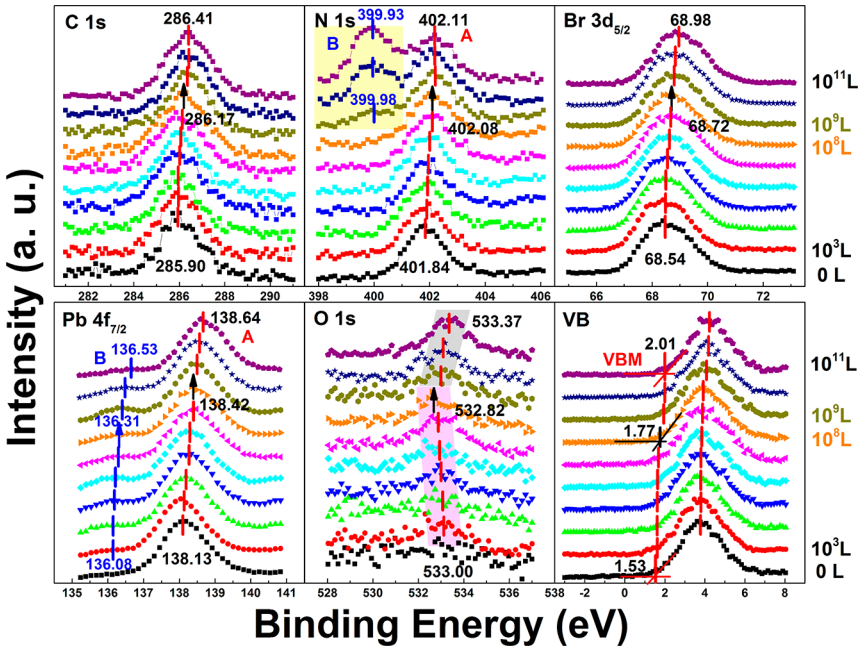

Figure 3. Evolution of C 1s, N 1s, Br $3d_{5/2}$, Pb $4f_{7/2}$, O 1s, and the VB region under water exposure from 0 to 10^{11} L. The black arrows denote the peak positions at 10^8 L.

decomposed perovskite ratio was saturated at 10% within seven sets of HR-XPS scans under all three atmospheres, no matter when the decomposition started and how long the exposures were. This may be due to the fact that the 10% metallic lead layer covered the perovskite surface and prevented it from further degradation.

H_2O Exposure. The most concerned factor that triggers the degradation of hybrid perovskites is moisture. Therefore, we performed the H_2O exposure on $MAPbBr_3$ SC from 0 to 10^{11} L (10 h HR-XPS scan). Because of the limitation of the equipment, we exposed the sample directly to 10^3 L as the second step. The humidity level in the exposure chamber during the water exposure was 100%. The evolution of C 1s, N 1s, Br $3d_{5/2}$, Pb $4f_{7/2}$, O 1s, and the VB region is shown in Figure 3. There were also two stages during the water exposure process. Before 10^8 L of exposure in the first stage, there was a rigid shift of ~0.24 eV to the higher BE of C 1s, N 1s, Br $3d_{5/2}$, and Pb $4f_{7/2}$ peaks. This rigid shift indicates that H_2O acted as the n dopant and moved the Fermi level of the crystal from 1.53 to 1.77 eV from VBM. The Pb-B peak which showed up at ~136.08 eV from the second scan can be attributed to X-ray degradation. The O 1s peak from the freshly cleaved sample was too weak to be detected. The O 1s peak that started to show up from 10^3 L at ~533.00 eV is ascribed to H_2O. It shifted to the lower BE position with a maximum of ~0.18 eV at 10^8 L. The opposite shifting direction suggests that there was no chemical reaction between H_2O and $MAPbBr_3$ at this stage.

We further analyzed the atomic ratio at each step and summarize the evolution in Figure 4 and Table 2. The ratio of the as-cleaved crystal is C/N/Pb/Br/O = 1.53:1.10:1:2.92:0. At the end of the first stage (10^8 L of H_2O, 7 h HR-XPS scan), the same 10% ratio of Pb from perovskite degraded into metallic Pb, as the net change in the test spot under 7 h of X-ray exposure. However, C 1s, N 1s, and Br $3d_{5/2}$ decreased by ~30, 37, and 27%. The 14% increase in O 1s came from the doped water. By carefully examining the ratio change, we suggest the

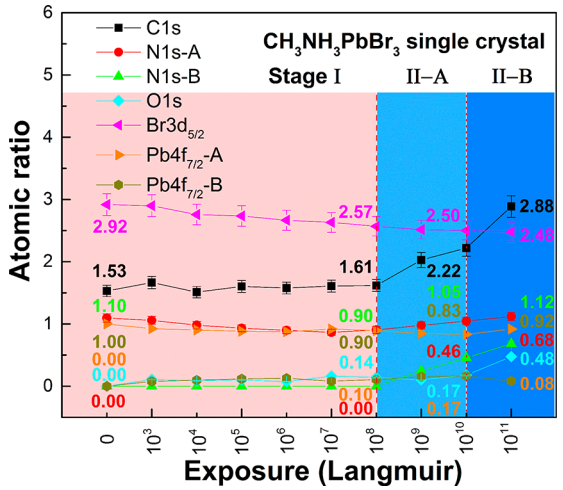

Figure 4. Elemental ratio comparisons of the perovskite single crystal during the water exposures in two stages with error bars.

following degradation mechanism in addition to eq 1 in water exposure stage I.

$$CH_3NH_3Br \xrightarrow{H_2O,X\text{-}ray} CH_3NH_2 \uparrow + HBr \uparrow \text{ (in UHV)} \quad (2)$$

With 14% doped water and X-rays, ~30% MABr from the diffusion process and the X-ray degradation reaction further degraded to CH_3NH_2 and HBr gases and then left the surface.

The second stage started from 10^9 L, where the SC began to react with H_2O as two obvious changes are shown in Figure 3. First, a second nitrogen peak (N 1s-B) at ~399.98 eV showed up, which may be ascribed to NH^{4+} resulting from the reaction between NH_3 and H_2O. It shifted in the lower BE direction ~0.05 eV, while N 1s-A from perovskite kept shifting to the higher BE direction until reaching ~402.11 eV at 10^{11} L. Second, the O 1s quickly shifted ~0.55 eV in the higher BE direction, which was opposite from that before 10^8 L but the same as for the other main peaks. The O 1s peak at ~533.37 eV

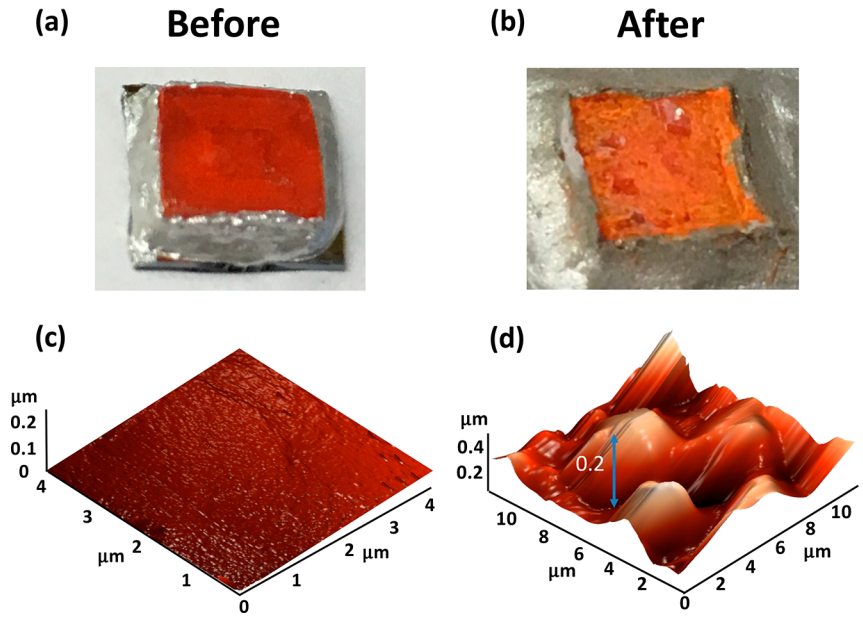

Figure 5. $MAPbBr_3$ single crystal (a) before and (b) after water exposure. Three-dimensional AFM images of the crystal surface (c) before and (d) after water exposure. The test areas are 4 μm × 4 μm and 10 μm × 10 μm, respectively.

(10^{11} L) may come from −OH. VBM and other peaks, C 1s, Br $3d_{5/2}$, Pb-A, and Pb-B, all shifted to the higher BE of ∼0.24 eV during this period. These results strongly demonstrate that the perovskite SC started to decompose because of water in the second stage. The HR-XPS spectral comparisons of the survey scan, cutoff region, and valence band region before and after 10^{11} L of H_2O exposure can be found in Figures S8 and S9. Given the band gap of the crystal as 2.3 eV, the Fermi level was brought very close to the bottom of the conduction band (0.29 eV, very n-type) after the exposure. The detailed HR-XPS spectral fittings of N 1s-A and N 1s-B, and Pb-A and Pb-B can be found in Figures S10 and S11, respectively.

The atomic ratio evolution in stage II-A as shown in Figure 4 revealed that Pb-B increased 17%, which is ∼7% higher than the 10% saturation ratio under the same X-ray exposure condition. The extra metallic lead may come from the X-ray degradation of $PbBr_2$, the product of the reaction between $MAPbBr_3$ and water. In stage II-B, however, the atomic ratio of metallic lead dropped ∼0.09, while O 1s further increased to 0.48. The calculation in Table 2 shows that C 1s increased ∼40% and N 1s and Br $3d_{5/2}$ decreased ∼39 and 32%, respectively, at the 10^{11} L exposure level. Therefore, we propose the following reactions in stage II:

$$CH_3NH_3PbBr_3 \xrightarrow{H_2O} (-CH_2-) + HBr\uparrow + NH_3\uparrow + PbBr_2 \quad \text{(in UHV)} \tag{3}$$

$$PbBr_2 \xrightarrow{\text{X-ray}} Pb + Br_2\uparrow \tag{4}$$

$$2Pb + 2H_2O + O_2 \rightarrow 2Pb(OH)_2\downarrow \tag{5}$$

$(-CH_2-)$ represents the hydrocarbon complex. A similar degradation mechanism of the $MAPbI_3$ thin films as shown in eq 3 can be found in Li. et al.'s work.[25] About 35% perovskite was degraded by water and released HBr and NH_3 gases in UHV. Partial NH_3 gas was absorbed by water, while $PbBr_2$ was further degraded into metallic lead and Br_2. From stage II-B, ∼0.09 metallic lead reacted with water and the residual O_2 in the chamber to form white precipitate $Pb(OH)_2$.

In conclusion, H_2O worked as an n dopant only in stage I and started to react with perovskite in stage II. The comparisons in Figure 5a,b further confirmed the existence of white precipitate $Pb(OH)_2$ as proposed in eq 5. The crystal was clear and shiny before the exposure but lost its transparency and mirrorlike surface afterward. The color also changed from dark red to light orange. In Figure 5c,d, we also compared the morphology measured by AFM. The average root-mean-square (RMS) roughness of the as-cleaved crystal was as small as 3.836 nm, indicating a very smooth surface. However, the value increased to 96.346 nm after the exposure, and the average height of the aggregated particles is as high as 0.2 μm. As we expected, water damaged the crystal surface severely after 10^{11} L of exposure.

To estimate the thickness of the decomposed layer and the lower limit of the decomposed region, we applied a simplified model as follows[23]

$$I_d = \int_0^d I_0 e^{-x/\lambda} dx = I_0\lambda(1 - e^{-d/\lambda}) \tag{6}$$

where I_0 and I_d correspond to the unit photoelectron emission intensity density and the intensity at a given thickness of d, respectively. λ is the electron mean free path. The photoelectron intensity was calculated on the basis of the peak area and the atomic sensitivity factors. Here, we assumed that the outer layer was completely decomposed and the underlying layer was still intact. With the thickness of the decomposed layer as d and the thickness of the crystal as d_0, the ratio of the intensities of two layers was given by

$$\frac{I_d}{I_{d_0}} = \frac{1 - e^{-d/\lambda}}{1 - e^{-d_0/\lambda}} \tag{7}$$

Thus,

$$d = -\lambda \ln\left[1 - \frac{I_d}{I_{d_0}}(1 - e^{-d_0/\lambda})\right] \tag{8}$$

with d_0 = 3.5 mm, λ = 2.0 nm, the intensity ratio of metallic Pb and the total Pb under X-ray exposure $I_{d_{X\text{-}ray}}/I_d$ = 0.10, a degradation thickness of $d_{X\text{-}ray}$ = 0.21 nm, the intensity ratio of metallic Pb, the total Pb after 10^{10} L of water exposure $I_{d_{H2O}}/I_d$ = 0.17, and a degradation thickness of d_{H_2O} = 0.37 nm.

It is worth mentioning that these results are rough estimations since neither the thickness nor the composition of the crystal surface was homogeneous during the degradation. However, they still could explain the discrepancy in the observations from photoluminescence (PL). Obviously, the degradations are merely limited at the surface even with ion diffusion from the bulk. PL, on the other hand, normally characterizes the material at a thickness of a few hundred nanometers depending on the absorption coefficient. In the water exposure case, it is possible that the bulk crystal is still intact with some physisorption of H_2O molecules and shows reversible photoelectrical properties.[20] However, the lattice-distortion-induced reconstruction of the SC observed by PL[53] still confirmed the doping of the H_2O molecules as we discussed above.

The metallic lead that showed up under X-ray exposure could act as the quenching centers of excitons,[54] but would not be easily formed under the ambient condition due to the large amount of O_2.[16] In addition, multiple groups have tried to use encapsulation techniques for small-area devices.[17] Other methods, such as adding different small molecules to passivate the $MAPbBr_3$ SC,[55] are still in the premature stages.

■ CONCLUSIONS

We have studied the in situ cleaved $MAPbBr_3$ single crystal degradation processes in X-ray, N_2, O_2, and H_2O atmospheres quantitatively and systematically at the surface level (<2 nm). X-ray degradation is inevitable if the sample is tested with HR-XPS. However, N_2 can protect the crystal from X-ray damage for 9 h. Also, both N_2 and O_2 acted as p-type dopants during N_2 and O_2 exposures. The difference is that N_2 was physically absorbed and slowly escaped the crystal surface afterward, but O_2 was able to bond with C to form C−O. As for the water exposure, H_2O worked as an n-type dopant in stage I (before 10^8 L) and started to react with perovskite surface within top 0.37 nm in stage II. By carefully controlling exposure levels, we revealed the detailed electronic structure and composition changes of the crystal surface. We believe our work provides insights into the degradation mechanisms and the key factors to fabricate high-quality perovskite single crystals and thus paves the way toward high-efficiency solar cells.

■ ASSOCIATED CONTENT

Supporting Information

The Supporting Information is available free of charge on the ACS Publications website at DOI: 10.1021/acs.jpcc.7b12740.

Single-crystal cleavage preparation. SEM and EDX comparisons. Evolutions of HRXPS spectra of cleaved samples under X-ray, N_2, O_2, and H_2O exposures. Electronic structure comparisons after H_2O exposure. Table of atomic ratios of as-cleaved crystals. (PDF)

■ AUTHOR INFORMATION

Corresponding Author

*E-mail: ygao@pas.rochester.edu.

ORCID

Congcong Wang: 0000-0003-4556-577X

Jinsong Huang: 0000-0002-0509-8778

Notes

The authors declare no competing financial interest.

■ ACKNOWLEDGMENTS

The authors are grateful for financial support from the National Science Foundation (grant nos. CBET-1437656 and DMR-1303742). J.H. acknowledges financial support from the National Science Foundation under the award of OIA-1538893. Technical support from the XRD Center in Mechanical Department and the Nanocenter at the University of Rochester is greatly appreciated.

■ REFERENCES

(1) Kojima, A.; Teshima, K.; Shirai, Y.; Miyasaka, T. Organometal Halide Perovskites as Visible-Light Sensitizers for Photovoltaic Cells. *J. Am. Chem. Soc.* **2009**, *131*, 6050−6051.

(2) Etgar, L.; Gao, P.; Xue, Z.; Peng, Q.; Chandiran, A. K.; Liu, B.; Nazeeruddin, M. K.; Grätzel, M. Mesoscopic $CH_3NH_3PbI_3/TiO_2$ Heterojunction Solar Cells. *J. Am. Chem. Soc.* **2012**, *134*, 17396−17399.

(3) Liu, M.; Johnston, M. B.; Snaith, H. J. Efficient Planar Heterojunction Perovskite Solar Cells by Vapour Deposition. *Nature* **2013**, *501*, 395−398.

(4) Xiao, Z.; Bi, C.; Shao, Y.; Dong, Q.; Wang, Q.; Yuan, Y.; Wang, C.; Gao, Y.; Huang, J. Efficient, High Yield Perovskite Photovoltaic Devices Grown by Interdiffusion of Solution-Processed Precursor Stacking Layers. *Energy Environ. Sci.* **2014**, *7*, 2619−2623.

(5) Jeon, N. J.; Noh, J. H.; Yang, W. S.; Kim, Y. C.; Ryu, S.; Seo, J.; Seok, S. I. Compositional Engineering of Perovskite Materials for High-Performance Solar Cells. *Nature* **2015**, *517*, 476−480.

(6) Wang, C.; Liu, X.; Wang, C.; Xiao, Z.; Bi, C.; Shao, Y.; Huang, J.; Gao, Y. Surface Analytical Investigation on Organometal Triiodide Perovskite. *J. Vac. Sci. Technol., B: Nanotechnol. Microelectron.: Mater., Process., Meas., Phenom.* **2015**, *33*, 032401.

(7) Son, D.-Y.; Lee, J.-W.; Choi, Y. J.; Jang, I.-H.; Lee, S.; Yoo, P. J.; Shin, H.; Ahn, N.; Choi, M.; Kim, D. Self-Formed Grain Boundary Healing Layer for Highly Efficient $CH_3NH_3PbI_3$ Perovskite Solar Cells. *Nat. Energy* **2016**, *1*, 16081.

(8) National Renewable Energy Laboratory Best Research-Cell Efficiencies Www.Nrel.Gov/Ncpv/Images/Efficiency_Chart.Jpg (Accessed Jan. 18, 2018).

(9) Bi, C.; Shao, Y.; Yuan, Y.; Xiao, Z.; Wang, C.; Gao, Y.; Huang, J. Understanding the Formation and Evolution of Interdiffusion Grown Organolead Halide Perovskite Thin Films by Thermal Annealing. *J. Mater. Chem. A* **2014**, *2*, 18508−18514.

(10) Yang, J.; Siempelkamp, B. D.; Liu, D.; Kelly, T. L. Investigation of $CH_3NH_3PbI_3$ Degradation Rates and Mechanisms in Controlled Humidity Environments Using in Situ Techniques. *ACS Nano* **2015**, *9*, 1955−1963.

(11) Liu, X.; Wang, C.; Lyu, L.; Wang, C.; Xiao, Z.; Bi, C.; Huang, J.; Gao, Y. Electronic Structures at the Interface between Au and $CH_3NH_3PbI_3$. *Phys. Chem. Chem. Phys.* **2015**, *17*, 896−902.

(12) Ahn, N.; Son, D.-Y.; Jang, I.-H.; Kang, S. M.; Choi, M.; Park, N.-G. Highly Reproducible Perovskite Solar Cells with Average Efficiency of 18.3% and Best Efficiency of 19.7% Fabricated Via Lewis Base Adduct of Lead (Ii) Iodide. *J. Am. Chem. Soc.* **2015**, *137*, 8696−8699.

(13) Wang, C.; Wang, C.; Liu, X.; Kauppi, J.; Shao, Y.; Xiao, Z.; Bi, C.; Huang, J.; Gao, Y. Electronic Structure Evolution of Fullerene on $CH_3NH_3PbI_3$. *Appl. Phys. Lett.* **2015**, *106*, 111603.

(14) Tan, Z.-K.; Moghaddam, R. S.; Lai, M. L.; Docampo, P.; Higler, R.; Deschler, F.; Price, M.; Sadhanala, A.; Pazos, L. M.; Credgington, D. Bright Light-Emitting Diodes Based on Organometal Halide Perovskite. *Nat. Nanotechnol.* **2014**, *9*, 687−692.

(15) Li, X.; Bi, D.; Yi, C.; Décoppet, J.-D.; Luo, J.; Zakeeruddin, S. M.; Hagfeldt, A.; Grätzel, M. A Vacuum Flash−Assisted Solution Process for High-Efficiency Large-Area Perovskite Solar Cells. *Science* **2016**, *353*, 58−62.
(16) Wei, H.; Fang, Y.; Mulligan, P.; Chuirazzi, W.; Fang, H.-H.; Wang, C.; Ecker, B. R.; Gao, Y.; Loi, M. A.; Cao, L. Sensitive X-Ray Detectors Made of Methylammonium Lead Tribromide Perovskite Single Crystals. *Nat. Photonics* **2016**, *10*, 333−339.
(17) Wang, D.; Wright, M.; Elumalai, N. K.; Uddin, A. Stability of Perovskite Solar Cells. *Sol. Energy Mater. Sol. Cells* **2016**, *147*, 255−275.
(18) Li, X.; Dar, M. I.; Yi, C.; Luo, J.; Tschumi, M.; Zakeeruddin, S. M.; Nazeeruddin, M. K.; Han, H.; Grätzel, M. Improved Performance and Stability of Perovskite Solar Cells by Crystal Crosslinking with Alkylphosphonic Acid Ω-Ammonium Chlorides. *Nat. Chem.* **2015**, *7*, 703−711.
(19) You, J.; Meng, L.; Song, T.-B.; Guo, T.-F.; Yang, Y. M.; Chang, W.-H.; Hong, Z.; Chen, H.; Zhou, H.; Chen, Q. Improved Air Stability of Perovskite Solar Cells Via Solution-Processed Metal Oxide Transport Layers. *Nat. Nanotechnol.* **2016**, *11*, 75−81.
(20) Fang, H.-H.; Adjokatse, S.; Wei, H.; Yang, J.; Blake, G. R.; Huang, J.; Even, J.; Loi, M. A. Ultrahigh Sensitivity of Methylammonium Lead Tribromide Perovskite Single Crystals to Environmental Gases. *Sci. Adv.* **2016**, *2*, e1600534.
(21) Tian, Y.; Peter, M.; Unger, E.; Abdellah, M.; Zheng, K.; Pullerits, T.; Yartsev, A.; Sundström, V.; Scheblykin, I. G. Mechanistic Insights into Perovskite Photoluminescence Enhancement: Light Curing with Oxygen Can Boost Yield Thousandfold. *Phys. Chem. Chem. Phys.* **2015**, *17*, 24978−24987.
(22) Galisteo-López, J. F.; Anaya, M.; Calvo, M.; Míguez, H. Environmental Effects on the Photophysics of Organic−Inorganic Halide Perovskites. *J. Phys. Chem. Lett.* **2015**, *6*, 2200−2205.
(23) Li, Y.; Xu, X.; Wang, C.; Ecker, B.; Yang, J.; Huang, J.; Gao, Y. Light Induced Degradation of $CH_3NH_3PbI_3$ Hybrid Perovskite Thin Film. *J. Phys. Chem. C* **2017**, *121*, 3904−3910.
(24) Wang, C.; Li, Y.; Xu, X.; Wang, C.; Xie, F.; Gao, Y. Degradation of Co-Evaporated Perovskite Thin Film in Air. *Chem. Phys. Lett.* **2016**, *649*, 151−155.
(25) Li, Y.; Xu, X.; Wang, C.; Wang, C.; Xie, F.; Yang, J.; Gao, Y. Degradation by Exposure of Coevaporated $CH_3NH_3PbI_3$ Thin Films. *J. Phys. Chem. C* **2015**, *119*, 23996−24002.
(26) Burschka, J.; Pellet, N.; Moon, S.-J.; Humphry-Baker, R.; Gao, P.; Nazeeruddin, M. K.; Grätzel, M. Sequential Deposition as a Route to High-Performance Perovskite-Sensitized Solar Cells. *Nature* **2013**, *499*, 316−319.
(27) Niu, G.; Li, W.; Meng, F.; Wang, L.; Dong, H.; Qiu, Y. Study on the Stability of $CH_3NH_3PbI_3$ Films and the Effect of Post-Modification by Aluminum Oxide in All-Solid-State Hybrid Solar Cells. *J. Mater. Chem. A* **2014**, *2*, 705−710.
(28) Conings, B.; Drijkoningen, J.; Gauquelin, N.; Babayigit, A.; D'Haen, J.; D'Olieslaeger, L.; Ethirajan, A.; Verbeeck, J.; Manca, J.; Mosconi, E. Intrinsic Thermal Instability of Methylammonium Lead Trihalide Perovskite. *Adv. Energy Mater.* **2015**, *5*, 1500477.
(29) Li, Y.; Xu, X.; Wang, C.; Wang, C.; Xie, F.; Yang, J.; Gao, Y. Investigation on Thermal Evaporated $CH_3NH_3PbI_3$ Thin Films. *AIP Adv.* **2015**, *5*, 097111.
(30) Xiao, Z.; Yuan, Y.; Shao, Y.; Wang, Q.; Dong, Q.; Bi, C.; Sharma, P.; Gruverman, A.; Huang, J. Giant Switchable Photovoltaic Effect in Organometal Trihalide Perovskite Devices. *Nat. Mater.* **2015**, *14*, 193−198.
(31) Leijtens, T.; Eperon, G. E.; Pathak, S.; Abate, A.; Lee, M. M.; Snaith, H. J. Overcoming Ultraviolet Light Instability of Sensitized TiO_2 with Meso-Superstructured Organometal Tri-Halide Perovskite Solar Cells. *Nat. Commun.* **2013**, *4*, 2885.
(32) Lee, S.-W.; Kim, S.; Bae, S.; Cho, K.; Chung, T.; Mundt, L. E.; Lee, S.; Park, S.; Park, H.; Schubert, M. C. Uv Degradation and Recovery of Perovskite Solar Cells. *Sci. Rep.* **2016**, *6*, 38150.
(33) Nie, W.; Blancon, J.-C.; Neukirch, A. J.; Appavoo, K.; Tsai, H.; Chhowalla, M.; Alam, M. A.; Sfeir, M. Y.; Katan, C.; Even, J. Light-Activated Photocurrent Degradation and Self-Healing in Perovskite Solar Cells. *Nat. Commun.* **2016**, *7*, 11574.
(34) Wang, S.; Jiang, Y.; Juarez-Perez, E. J.; Ono, L. K.; Qi, Y. Accelerated Degradation of Methylammonium Lead Iodide Perovskites Induced by Exposure to Iodine Vapour. *Nat. Energy* **2016**, *2*, 16195.
(35) Edri, E.; Kirmayer, S.; Cahen, D.; Hodes, G. High Open-Circuit Voltage Solar Cells Based on Organic−Inorganic Lead Bromide Perovskite. *J. Phys. Chem. Lett.* **2013**, *4*, 897−902.
(36) Heo, J. H.; Song, D. H.; Im, S. H. Planar $CH_3NH_3PbBr_3$ Hybrid Solar Cells with 10.4% Power Conversion Efficiency, Fabricated by Controlled Crystallization in the Spin-Coating Process. *Adv. Mater.* **2014**, *26*, 8179−8183.
(37) Yang, Y.; Yan, Y.; Yang, M.; Choi, S.; Zhu, K.; Luther, J. M.; Beard, M. C. Low Surface Recombination Velocity in Solution-Grown $CH_3NH_3PbBr_3$ Perovskite Single Crystal. *Nat. Commun.* **2015**, *6*, 7961.
(38) Wang, C.; Ecker, B. R.; Wei, H.; Huang, J.; Meng, J.-Q.; Gao, Y. Valence Band Dispersion Measurements of Perovskite Single Crystal with Angle-Resolved Photoemission Spectroscopy. *Phys. Chem. Chem. Phys.* **2017**, *19*, 5361−5365.
(39) Schmidt, L. C.; Pertegás, A.; González-Carrero, S.; Malinkiewicz, O.; Agouram, S.; Minguez Espallargas, G.; Bolink, H. J.; Galian, R. E.; Pérez-Prieto, J. Nontemplate Synthesis of $CH_3NH_3PbBr_3$ Perovskite Nanoparticles. *J. Am. Chem. Soc.* **2014**, *136*, 850−853.
(40) Baikie, T.; Fang, Y.; Kadro, J. M.; Schreyer, M.; Wei, F.; Mhaisalkar, S. G.; Graetzel, M.; White, T. J. Synthesis and Crystal Chemistry of the Hybrid Perovskite ($CH_3NH_3PbI_3$) for Solid-State Sensitised Solar Cell Applications. *J. Mater. Chem. A* **2013**, *1*, 5628−5641.
(41) Ohmann, R.; Ono, L. K.; Kim, H.-S.; Lin, H.; Lee, M. V.; Li, Y.; Park, N.-G.; Qi, Y. Real-Space Imaging of the Atomic Structure of Organic−Inorganic Perovskite. *J. Am. Chem. Soc.* **2015**, *137*, 16049−16054.
(42) Wei, H.; DeSantis, D.; Wei, W.; Deng, Y.; Guo, D.; Savenije, T. J.; Cao, L.; Huang, J. Dopant Compensation in Alloyed $CH_3NH_3PbBr_{3-x}Cl_x$ Perovskite Single Crystals for Gamma-Ray Spectroscopy. *Nat. Mater.* **2017**, *16*, 826−833.
(43) Liu, Y.; Yang, Z.; Cui, D.; Ren, X.; Sun, J.; Liu, X.; Zhang, J.; Wei, Q.; Fan, H.; Yu, F. Two-Inch-Sized Perovskite $CH_3NH_3PbX_3$ (X= Cl, Br, I) Crystals: Growth and Characterization. *Adv. Mater.* **2015**, *27*, 5176−5183.
(44) Mashiyama, H.; Kawamura, Y.; Magome, E.; Kubota, Y. Displacive Character of the Cubic-Tetragonal Transition in $CH_3NH_3PbX_3$. *J. Korean Phys. Soc.* **2003**, *42*, S1026−S1029.
(45) Gao, Y. Surface Analytical Studies of Interfaces in Organic Semiconductor Devices. *Mater. Sci. Eng., R* **2010**, *68*, 39−87.
(46) Liu, X.; Yi, S.; Wang, C.; Wang, C.; Gao, Y. Electronic Structure Evolution and Energy Level Alignment at C_{60}/4, 4′-Cyclohexylidene-bis [N, N-Bis (4-Methylphenyl) Benzenamine]/MoO_x/Indium Tin Oxide Interfaces. *J. Appl. Phys.* **2014**, *115*, 163708.
(47) Liu, X.; Wang, C.; Wang, C.; Irfan, I.; Gao, Y. Interfacial Electronic Structures of Buffer-Modified Pentacene/C_{60}-Based Charge Generation Layer. *Org. Electron.* **2015**, *17*, 325−333.
(48) Hinckley, A. C.; Wang, C.; Pfattner, R.; Kong, D.; Zhou, Y.; Ecker, B.; Gao, Y.; Bao, Z. Investigation of a Solution-Processable, Nonspecific Surface Modifier for Low Cost, High Work Function Electrodes. *ACS Appl. Mater. Interfaces* **2016**, *8*, 19658−19664.
(49) Wei, W.; Zhang, Y.; Xu, Q.; Wei, H.; Fang, Y.; Wang, Q.; Deng, Y.; Li, T.; Gruverman, A.; Cao, L. Monolithic Integration of Hybrid Perovskite Single Crystals with Heterogenous Substrate for Highly Sensitive X-Ray Imaging. *Nat. Photonics* **2017**, *11*, 315−321.
(50) Dong, X.; Fang, X.; Lv, M.; Lin, B.; Zhang, S.; Ding, J.; Yuan, N. Improvement of the Humidity Stability of Organic−Inorganic Perovskite Solar Cells Using Ultrathin Al_2O_3 Layers Prepared by Atomic Layer Deposition. *J. Mater. Chem. A* **2015**, *3*, 5360−5367.
(51) Wang, Y. K.; Yuan, Z. C.; Shi, G. Z.; Li, Y. X.; Li, Q.; Hui, F.; Sun, B. Q.; Jiang, Z. Q.; Liao, L. S. Dopant-Free Spiro-Triphenylamine/Fluorene as Hole-Transporting Material for Perovskite Solar

Cells with Enhanced Efficiency and Stability. *Adv. Funct. Mater.* **2016**, *26*, 1375−1381.
(52) Zhu, Z.; Hadjiev, V. G.; Rong, Y.; Guo, R.; Cao, B.; Tang, Z.; Qin, F.; Li, Y.; Wang, Y.; Hao, F. Interaction of Organic Cation with Water Molecule in Perovskite $MAPbI_3$: From Dynamic Orientational Disorder to Hydrogen Bonding. *Chem. Mater.* **2016**, *28*, 7385−7393.
(53) Murali, B.; Dey, S.; Abdelhady, A. L.; Peng, W.; Alarousu, E.; Kirmani, A. R.; Cho, N.; Sarmah, S. P.; Parida, M. R.; Saidaminov, M. I. Surface Restructuring of Hybrid Perovskite Crystals. *ACS Energy Lett.* **2016**, *1*, 1119−1126.
(54) Sadoughi, G.; Starr, D. E.; Handick, E.; Stranks, S. D.; Gorgoi, M.; Wilks, R. G.; Bär, M.; Snaith, H. J. Observation and Mediation of the Presence of Metallic Lead in Organic−Inorganic Perovskite Films. *ACS Appl. Mater. Interfaces* **2015**, *7*, 13440−13444.
(55) Murali, B.; Yengel, E.; Yang, C.; Peng, W.; Alarousu, E.; Bakr, O. M.; Mohammed, O. F. The Surface of Hybrid Perovskite Crystals: A Boon or Bane. *ACS Energy Lett.* **2017**, *2*, 846−856.